CARDIFF UNIVERSITY
PRIFYSGOL CAERDYDD

ORCA – Online Research @ Cardiff

This is an Open Access document downloaded from ORCA, Cardiff University's institutional repository:https://orca.cardiff.ac.uk/id/eprint/133556/

This is the author's version of a work that was submitted to / accepted for publication.

Citation for final published version:

Gong, Yongkang, Wong, Stephan, Bennett, Anthony J. , Huffaker, Diana L. and Oh, Sang Soon 2020. Topological insulator laser using valley-hall photonic crystals. ACS Photonics 7 (8) , pp. 2089-2097. 10.1021/acsphotonics.0c00521

Publishers page: https://doi.org/10.1021/acsphotonics.0c00521

Please note:
Changes made as a result of publishing processes such as copy-editing, formatting and page numbers may not be reflected in this version. For the definitive version of this publication, please refer to the published source. You are advised to consult the publisher's version if you wish to cite this paper.

This version is being made available in accordance with publisher policies. See http://orca.cf.ac.uk/policies.html for usage policies. Copyright and moral rights for publications made available in ORCA are retained by the copyright holders.

Topological Insulator Laser Using Valley-Hall Photonic Crystals

Yongkang Gong[†], Stephan Wong[†], Anthony J. Bennett[‡], Diana L. Huffaker[†], and Sang Soon Oh[†,]*

[†]School of Physics and Astronomy, Cardiff University, Cardiff, CF24 3AA, United Kingdom.
[‡]School of Engineering, Cardiff University, Cardiff, CF24 3AA, United Kingdom.

ABSTRACT: Topological photonics has recently been proved a robust framework for manipulating light. Active topological photonic systems, in particular, enable richer fundamental physics by employing nonlinear light-matter interactions, thereby opening a new landscape for applications such as topological lasing. Here we propose an all-dielectric topological insulator laser scheme in telecommunication region based on semiconductor cavities formed by topologically distinct Kagome photonic crystals. Our theoretical results show that the proposed planar semiconductor Kagome lattice can lift degeneracy with geometrical perturbation and open broad photonic bandgaps, and valley-dependent edge states and topologically robust transport with subwavelength scale confinement are observed at the edge of the perturbed Kagome lattices with distinct valley Chern numbers. An interesting feature of the Kagome lattices is that it supports two different types of valley Hall edge modes, which enables the coexistence of high Q ring-resonator modes and lossy Fabry–Pérot resonator modes in the proposed topological cavities. Moreover, we explore pumping and lasing dynamics of the topological cavities by means of a four-level two-electron model and demonstrate that this model offers a powerful platform to investigate non-Hermitian topological laser cavities with arbitrary geometry. The proposed topological semiconductor scheme provides a new route to study non-Hermitian topological photonics and to develop integrated topological systems for robust light generation and transport.

KEYWORDS: *photonic topological insulators, edge states, lasers, photonic crystals*

INTRODUCTION

Transplanting the concept of topological phase transitions in fermionic systems to photonics has recently attracted enormous interest.[1-3] In contrast to conventional photonic defect states that are sensitive to perturbations, edge states from two topologically distinct regions in photonic topological insulators (PTIs) are robust against local perturbations and immune to back scattering, which could lead to intriguing and unexpected photonic devices and functionalities for robust electromagnetic wave transport and processing.[4-7] Implementations of PTIs vary considerably and several schemes have been developed. For example, photonic analogue of a quantum Hall topological insulator was first achieved in the microwave regime using gyromagnetic materials with a strong magnetic field applied to break the time-reversal symmetry.[8] Later, a number of proposals have been put forward to realize photonic topological transport free of external fields by temporal modulation of photonic crystals to mimic time-reversal-symmetry breaking.[9-12] A subwavelength-scale PTI approach via pseudo-time-reversal symmetry in all-dielectric photonic crystals was recently proposed[13] and experimentally verified from visible wavelengths to microwave regime.[14-18] Another elegant subwavelength-scale nontrivial topology strategy has been introduced by exploiting the optical valley Hall effect to break spatial-inversion symmetry to access the opposite Berry curvature near Brillouin zone corners.[19-28] which opens avenues to on-chip photonic devices for robust topologically protected light manipulation.

In addition to above passive PTIs researches, a considerable effort has been made towards the study of non-Hermitian PTIs by engaging edge states with optical nonlinearity to enable topological lasing. In contrast to the conventional laser technologies, which are generally sensitive to cavity deformations caused by fabrication imperfections and fluctuations, topological insulator laser cavities are potentially immune to certain cavity defects with higher lasing efficiency attributed to the unique characteristics of nontrivial edge states. Topological

insulator laser was first experimentally reported in magneto-optical photonic crystals pumped by a static magnetic field to break time-reversal symmetry.[29] Although this approach allows nonreciprocal lasing from topological cavities of arbitrary geometries, it produces narrow topological bandgap due to weak magneto-optic effect in optical regime. Non-magnetic topologically protected edge-mode lasing was later proposed and implemented by nontrivial semiconductor ring-resonator arrays, and high efficiency single mode lasing that is robust to cavity defects/disorders was reported.[30, 31] The one-dimensional Su-Schrieffer-Heeger (SSH) hamiltonian model is another popular approach to generate edge states and various types of SSH lasing devices have been recently demonstrated based on micro-ring resonators,[32, 33] electrically injected Fabry-Perot chain,[34] semiconductor pillar arrays,[35] and photonic crystal nanocavities.[36, 37] Very recently, a topological single mode laser based on bulk topological effect was reported.[38] A topological laser arising from the valley Hall edge state was theoretically suggested.[39] The electrically pumped topological laser with valley edge modes was first experimentally achieved in THz regime using quasi-hexagonal photonic crystals.[40]

In this paper, we propose a new kind of all-dielectric photonic topological laser in telecommunication region based on Kagome valley-hall photonic-crystals (KVPs) that consist of hexagonal lattice with primitive cells containing three nanoholes in compound semiconductor membrane. Our analytical and numerical investigations demonstrate that the proposed KVPs concept can lift degeneracy at K point with geometrical perturbation and open broad photonic bandgaps. Valley-dependent edge states and topologically robust transport with subwavelength scale confinement are observed at the interface between two perturbed KVPs with different valley Chern numbers. We further construct topological laser cavities with triangular geometry and explore pumping and lasing dynamics of the topological cavities by means of a four-level two-electron model. Our demonstration of lasing from the proposed KVPs scheme could provide opportunities for engineering topological edge states for various

passive and active photonic integrated devices and systems.

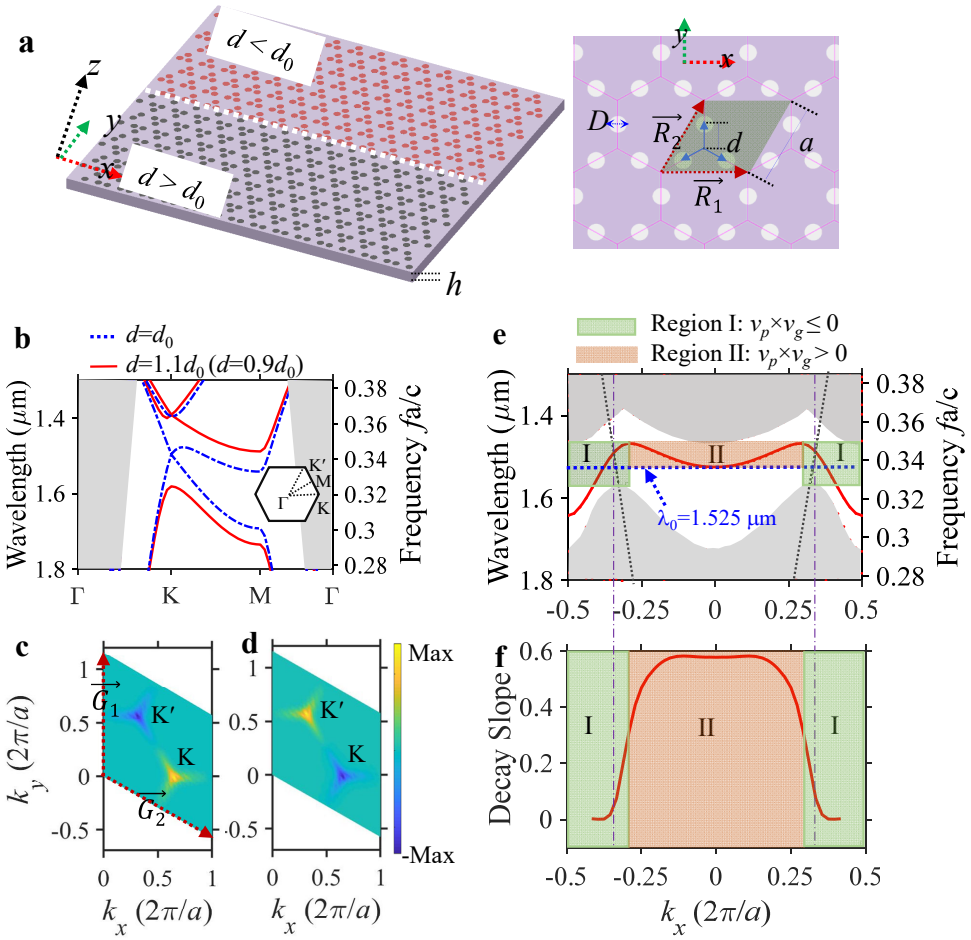

Figure 1. Band structure and topology analysis of the proposed all-dielectric KVPs on InGaAsP membrane. **a** Schematic diagram of the perturbed KVPs (left) and top view of the KVPs (right) indicating primitive cell that contains three holes with unit vectors of $\overrightarrow{R_1}$ and $\overrightarrow{R_2}$ and lattice constant length of a. The positive and negative perturbation occurs at spacing $d>d_0$ and $d<d_0$ ($d_0 = \frac{a}{2\times\sqrt{3}}$), respectively. **b** Band structure of the unperturbed (blue line) and perturbed (red line) KVPs. The grey region represents light cone. **c**, **d** Valley dependent Berry curvature of the first band of the negatively and positively perturbed KVPs in the reciprocal primitive unit cell, respectively. $\overrightarrow{G_1}$ and $\overrightarrow{G_2}$ are the reciprocal lattice vectors. **e** Projected band structure of the topological waveguide in **a**. **f** Decay slope of the edge states of the topological waveguide. In **e** and **f**, the black dashed line represents light lines, the purple perpendicular dashed lines indicate the wavelengths that the light lines and the edge dispersion curve cross, and the blue parallel dotted line shows edge mode wavelength λ_0=1.525 μm at k_x=0. The geometrical parameters in above designs are slab height h=170 nm, lattice length a=500 nm, and hole diameter D=150 nm. The unperturbed KVPs has $d=d_0$=144 nm, while the positively and negatively perturbed KVPs have $d=1.1d_0$ and $d=0.9d_0$, respectively. The refractive index of InGaAsP material is 3.3.[41]

Results

Topological properties of the KVPs. The proposed all-dielectric topological strategy is based on hole array KVPs on high refractive index InGaAsP membrane, which has hexagonal lattice with primitive cell composed of three nanoholes with identical diameters D, as schematically depicted in Figure 1a. Perturbation to retrieve nontrivial KVPs can be introduced by putting the three nanoholes closer (negative perturbation) or further away (positive perturbation) from each other. When the hole-to-center spacing d equals to $d_0 = \frac{a}{2\times\sqrt{3}}$, the KVPs are typical Kagome photonic crystal with C_6 symmetry, featuring a Dirac cone at K and K′ points in the momentum space as indicated by the TE-like band structure (Figure 1b). When we introduce positive perturbation by varying d=d_0 to d=1.1d_0 or negative perturbation by varying d=d_0 to d=0.9d_0, we break the inversion symmetry and reduce the lattice symmetry to C_3 symmetry. As a result, the degeneracy at the K (K′) point is lifted and a band gap opens. Although the positively and negatively perturbed KVPs show the same band structure (Figure 1b) due to the geometrical equivalence, they produce 180 degree-rotated Berry curvature profile because the K and K′ points are swapped under the rotation as illustrated in Figures 1c and 1d, respectively, where non-zero Berry curvature with opposite signs appears at the K and K′ points. We observe that the negatively perturbed KVPs have positive (negative) Berry curvature at K (K′), while the positively perturbed KVPs have negative (positive) Berry curvature at K (K′). As a result, the two types of KVPs have valley Chern numbers with different signs, thereby edge states are guaranteed at the geometric boundary between them. The band structure and Berry curvature results obtained from our tight binding approximation (Figure S2 and S3 in the Supporting Information) agree well with those in Figures 1b-1d.

Topological light routing. Thanks to the bulk-edge correspondence, we can achieve topological edge states at the boundary between the KVPs with positive and negative perturbation as shown in Figure 1a. Figure 1e reveals that edge states with wavelength range

of 1468 nm-1578 nm are generated within photonic bandgap. Moreover, edge states at wavelengths of 1500 nm-1578 nm are below light line, which guarantees broadband

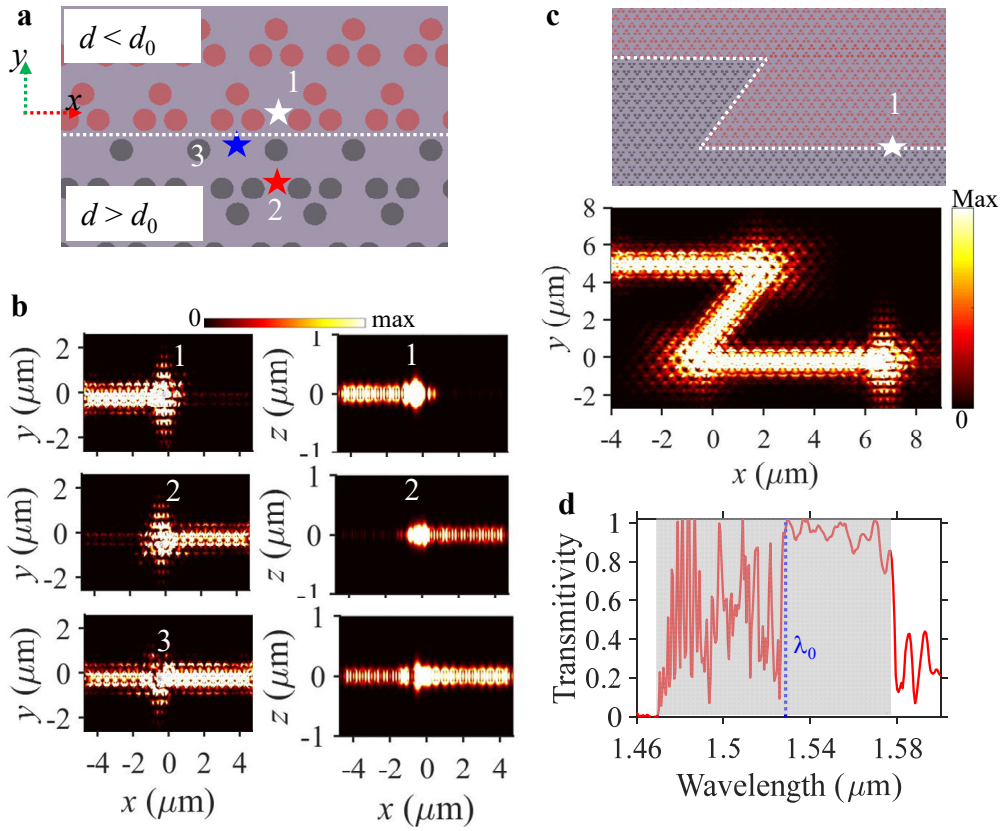

Figure 2. Light propagation and field distribution characteristics of the edge states. **a** Left-handed circular polarized dipoles (marked as star symbols) placed at different positions near the interface between the negatively and the positively perturbed KVPs to excite edge modes and **b** the corresponding field distribution $|E|^2$ of the edge mode at wavelength of 1550 nm in *xy* and *xz* planes. **c** Schematic of a Z-shaped topological waveguide (upper figure) and the corresponding field distribution $|E|^2$ at wavelength of 1550 nm (bottom figure). **d** Transmission spectra of the Z-shaped waveguide obtained by normalizing the Z-shaped waveguide to the straight waveguide (Figure S6 in Supporting Information). The shaded area indicates the wavelength range of the edge states. The white dashed lines in **c** and **d** indicate the boundary between the negatively and the positively perturbed KVPs. The geometric parameters in above designs are the same as those in Figure 1.

topologically protected light propagation with out-of-plane confinement. It is worth noting that the edge states can be categorized into two regions: region I ($v_p \times v_g \leq 0$) and region II ($v_p \times v_g > 0$), where v_p and v_g are phase velocity and group velocity, respectively. The wavelengths of two

regions overlap from 1.468 μm to 1.525 μm (denoted as λ_0) within photonic bandgap. We observe from Figure 1e that when edge mode wavelength is longer than λ_0, only single unidirectional edge mode within Region I can be excited at each wavelength in the light propagation direction of $+x$ or $-x$. When the edge mode wavelength is shorter than (or equal to) λ_0, however, dual unidirectional edge modes (one in Region I and the another in Region II) can be excited at each wavelength in the light propagation direction of $+x$ or $-x$. Above interesting features have not been demonstrated by the valley hall photonic crystals based on Kagome lattice reported in Ref. [28]. Figure 1f demonstrates that the edge modes below light line in Region I have smaller decay slop than others because of lower vertical light loss.

We investigate unidirectional propagation feature of the edge states in KVP waveguide as schematically shown in Figure 2a. Figure 2b shows that the same sources at different structure positions can excite unidirectional edge states propagating in the opposite direction due to chiral light matter interaction,[42] which is also observed in other reported photonic quantum spin Hall[13, 15, 16] and photonic quantum valley Hall systems.[26, 27] When left-handed circularly polarized source excites photons at locations "1" ("2"), negative (positive) chirality is predominant and leftward (rightward) unidirectional light propagation occurs. At location "3", the local electric fields of the edge mode are elliptically polarized and hence the light propagates in both left and right direction.[43, 44] In any case, the light is well confined at the boundary between the two perturbed KVPs in both *xy* and *xz* planes due to the presence of topological edge states below light line. We also evaluate field distribution and spectra in both Region I and Region II are excited in this case (as predicted in Figure 1e), and the intensity of the excited modes in the two regions varies significantly with wavelength under the same dipole source excitation.

Q factor and resonant modes of the KVP cavities. Based on the developed KVP scheme, we design a topological triangle cavity that consists of the negatively perturbed KVPs inside of the

cavity and the positively perturbed KVPs outside of the cavity, as depicted in Figure 3a. If the cavity is arranged in an opposite manner, i.e., the cavity inside is the positively perturbed KVPs

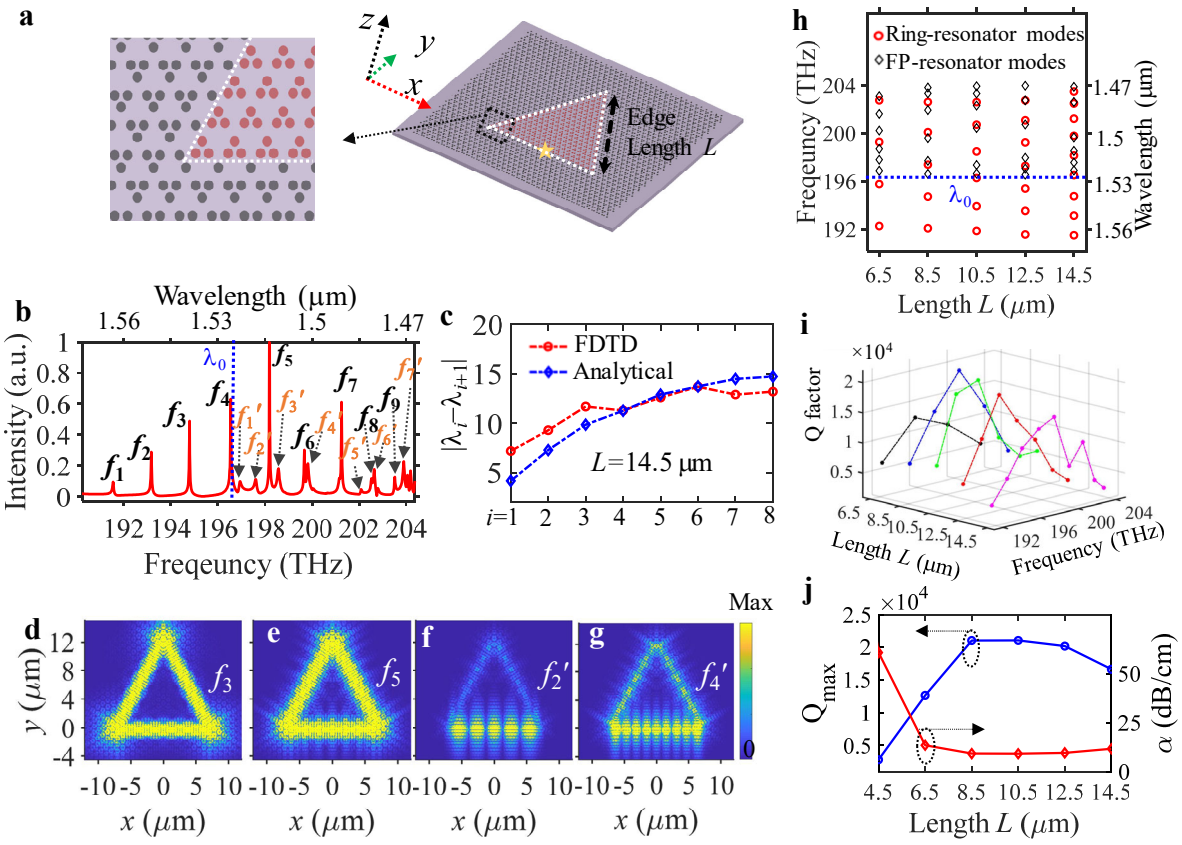

Figure 3. Optical properties of the proposed equilateral triangle KVP cavity. **a** Schematic diagram of the cavity (right) and the zoomed in cavity corner area (left). Red and black areas represent the negatively and positively perturbed KVPs, respectively, and the white dashed line indicate the boundary between them. The star symbol indicates the location where dipole sources are placed to excite cavity modes. **b** Optical spectra of the KVP cavity under cavity edge length of L=14.5 μm. **c** Numerically and analytically derived FSR of the ring-resonator modes. **d**, **e** Field distribution $|E|$ of the topological ring-resonator modes at frequencies of f_3=194.8 THz (λ_3=1539 nm) and f_5=198.2 THz (λ_5=1513 nm) at Z=0 μm plane, respectively. **f**, **g** Field distribution $|E|$ of the FP-resonator modes at frequencies of f_2'=197.6 THz and f_4'=199.8 THz, respectively. **h** Dependence of the frequencies of the resonant modes on cavity length. **i** Dependence of the ring-resonator modes' Q factor on cavity length. **j** The maximum Q factor (Q_{max}) and the propagation loss α of the edge modes versus cavity length. The geometrical parameters in the simulations are the same as those in Figure 2.

while the cavity outside is the negatively perturbed KVPs, the majority of the edge states lies

above the light line (see Figure S7 in Supporting Information). The proposed triangle cavity properties of topological waveguides with 120-degree bends. Figures 2c and 2d show that the topologically protected light propagates smoothly around sharp bends with high transmission. Spectral oscillation occurs at wavelengths shorter than λ_0=1.525 μm. It is because edge modes supports two types of resonant modes (i.e., ring-resonator modes and FP-resonator modes), which differs to the valley hall photonic crystal cavity reported in Ref. [40]. For example, when cavity edge length L is 14.5 μm, nine ring-resonator modes with frequencies of f_i (i=1, 2, …9) and seven FP (Fabry–Pérot) -resonator modes with frequencies of f_m' (m=1, 2, …7) appear, as shown in Figure 3b. The ring-resonator modes arise from excitation of low propagation loss edge modes within Region I (Figures 1e and 1f), which is evidenced by the E-field distributions showing that light propagates smoothly along the whole cavity (Figures 3d and 3e). In contrast to the ring-resonator modes, the FP-resonator modes experience high reflection from the cavity corners (Figures 3f and 3g). The FP-resonator modes originate from excitation of lossy edge modes in Region II (Figures 1e and 1d), which explains why the wavelengths of FP-resonator modes are shorter than λ_o as indicated in Figure 3b.

To further analyze the cavity modes, we perform free-spectral-range (FSR) calculations of the ring-resonator modes based on $\Delta\lambda_{FSR}=\lambda^2/(n_g L_{cavity})$,[45] where n_g is group index and L_{cavity} is the effective length of light propagating in the cavity. Numerical FSR results were obtained from FDTD results using $\Delta\lambda_{FSR}=|\lambda_i-\lambda_{i+1}|$ (i=1, 2, …8), where λ_i is the wavelength of i-th ring resonator modes. Figure 3c illustrates that the value of the FSR of the ring-resonator modes is not constant due to waveguide dispersion (i.e., n_g varies with wavelength). There is deviation between the analytically and the numerically obtained FSR, which arises from the fact that we approximate $L_{cavity}=3L$ in the numerical analysis. In fact, L_{cavity} should change with wavelength, since different ring-resonator modes have slightly different light field profile around cavity

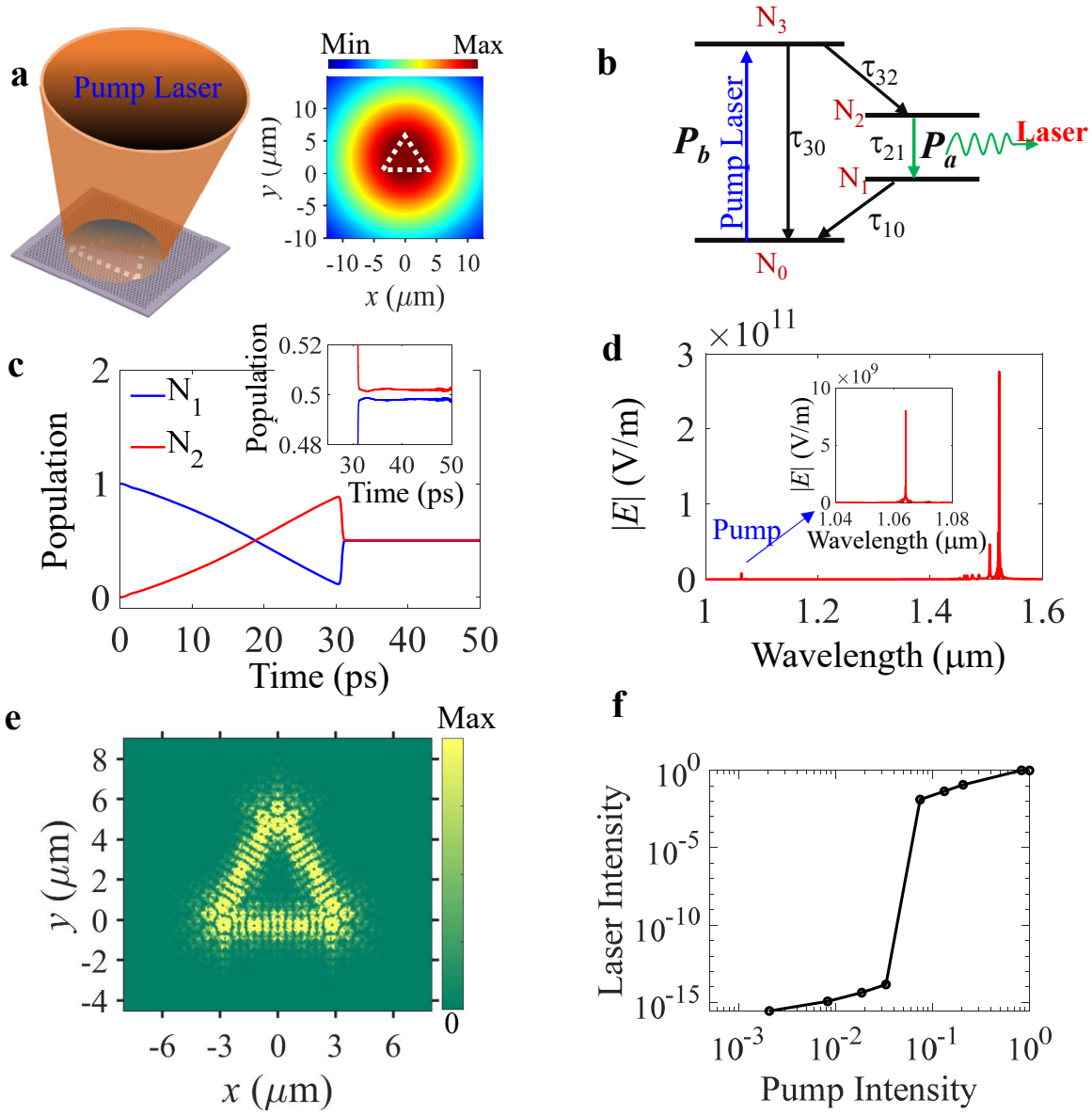

Figure 4. **Lasing characteristics of the proposed triangle cavity KVP lasers**. **a** Schematic of the cavity optically pumped by another laser from the top of it (left) and the spatial intensity profile of the pump laser with a Gaussian shape (right). The white dotted line represents the outline of the cavity edges. **b** Schematic diagram of the four-level two-electron model for the KVP lasers. **c** Evolution of electron population density probability with time at level N_1 and N_2. The inset shows population inversion when the lasing is stabilized. **d** Spectrum of the KVP laser. The inset is the spectrum of the pump laser at wavelength of 1064 nm. **e** Lasing field distribution $|E|$ of the cavity at edge mode wavelength of ~1523 nm at Z=0 μm plane. **f** Normalized output laser intensity versus normalized pump laser intensity. The cavity edge length in the simulations is L=6.5 μm and the other geometrical parameters are the same as those in Figure 3.

corners and thus yield different L_{cavity}. Furthermore, we study the dependence of the resonant modes' frequencies on the cavity length (Figure 3h). The frequency spacing of the ring-resonator modes decrease with L. We note that the FP-resonator modes always appear at wavelengths shorter than λ_0=1.525 μm, which prove that the physical origin of FP-resonator modes is excitation of the edge modes in Region II (Figures 1e and 1d). Figure 3i shows that for the same cavity length, the ring-resonator modes at the frequencies in the sides of the edge states range tend to have smaller Q factors than those for the frequencies in the middle of the edge states range, which is because they are close to bulk modes and have larger lateral losses. We observe that the maximum Q factor reaches 2.1×10^4 at wavelength of 1518.7 nm when the cavity edge length L=8.5 μm. The proposed cavity has higher Q factor than that of the recently reported topological ring resonator cavity based on photonic quantum spin hall effect.[18] Figure 3j demonstrates that the maximum Q factor depends on cavity length and decreases rapidly with the cavity length when L<8.5 μm, which is due to light in the cavity edges starting to couple from each other when the cavity edges become closer. We also note that the maximum Q factor drops when cavity length increases (L>8.5 μm) due to larger propagation loss of edge modes for longer cavity. We observe from Figure 3j that the propagation loss increases from ~9.16 dB/cm to ~11.6 dB/cm when L changes from 8.5 μm to 14.5 μm. The Q factor drops slowly because of the propagation loss of the modes below the light line (Figures 1e and 1f), which differs to the spin Hall-type photonic crystal cavities that have larger vertical loss and lower Q factor due to edge states above the light line.[18, 46] We study how the number of the periods of the surrounding photonic crystals m (Figure S8 in in the Supporting Information) affect the Q factor. We observe that the Q factor does not change much as long as m is large enough to confine the field of the edge modes near cavity edges. When m reduces, the field of the edge mods starts to decay to the ambient membrane through the surrounding photonic crystals and thereby the Q factor becomes smaller. We stress that estimating the light

propagation loss by the cavity Q factor is valid only when the size of surrounding PhCs is large enough to confine the field of the edge modes near the cavity edges. When the size of the surrounding PhCs is small, light leakage to the surrounding occurs and introduces additional optical loss apart from the propagation loss, and hence estimation of the propagation loss by Q factor will be inaccurate.

Topological laser cavities. We further study lasing performance of the topological cavity by introducing gain to the InGaAsP material and optically pumping the KVP cavity, as illustrated in Figure 4a. We utilize a four-level two-electron model to investigate lasing dynamics of the cavity, as described in Figure 4b. As an example, we simulate KVP cavities with edge length of L=6.5 μm. The electron populations of the levels rely on pumping intensity and spontaneous emission decay. We demonstrate that the population inversion of Level 2 relative to Level 1 can be achieved at pump laser intensity of $|E|=3\times10^5$ V/m (Figure 4c). Consequently, lasing at edge state wavelength of ~1523 nm is achieved, as shown from the laser spectrum and the field distribution in Figures 4d and 4e. The field profile looks slightly different to that in Figure 3d, because they are corresponding to different modes at different wavelengths. Figure 4f displays that the laser intensity experiences a dramatically jump when the power of the pump laser increases to a certain value and then becomes saturated when the pump laser further increases– a typical laser threshold behavior with a clear transition from spontaneous emission to stimulated emission.

Next, we investigate robustness of the proposed KVP lasers. We design a topological cavity with complex closed boundary between the perturbed KVPs (Figure 5a). Despite of a complex cavity geometry, distinct topological invariants of the two perturbed KVPs ensures the existence of topological laser modes, and the generated laser is well confined and propagates smoothly along the boundary (Figure 5b). We note from Figure 4d and Figure 5c that multiple lasing modes are excited, which is due to the fact that we use a relatively large value of

dephasing rate γ_a in our design so that the gain of the material covers broad edge states' wavelength range. As a result, when the pump laser power is strong, additional ring-resonator modes start to lase. The cavity has different cavity length to that in Figure 4 and hence generates resonate edge modes with different wavelengths. The lasing at the resonant mode wavelength of 1516 nm is dominant, which we think is due to this mode having higher gain and lower loss than the other resonant modes from the same cavity.

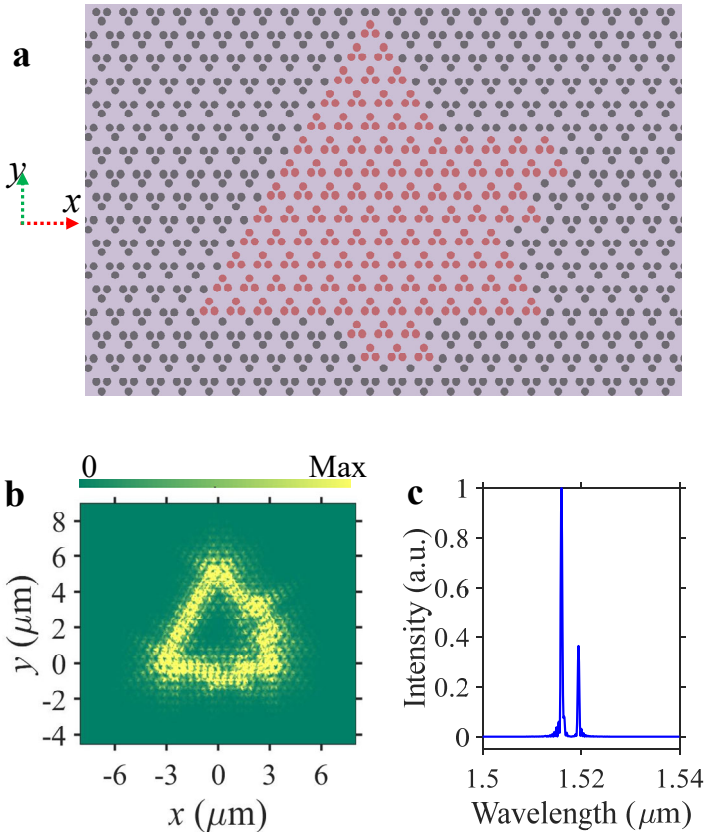

Figure 5. Topological insulator laser cavity with complex geometry. **a** Schematic top-view of the cavity. **b** Field distribution $|E|$ of the edge mode laser at wavelength of 1516 nm. **c** Spectrum of the laser cavity. The red and black regions in **a** indicate the negatively and positively perturbed KVPs, respectively. The geometrical parameters of the cavity are the same as those in Figure 4 except the cavity shape and length.

Discussion

Discovery of new types of non-trivial photonic topological platforms facilitates the development of novel topological lasers. We have demonstrated a PTI strategy based on all-dielectric hole-type Kagome lattice, which differs fundamentally to the recently reported

approaches based on quantum spin Hall effect,[29-31, 38] One advantage of the developed KVPs in the semiconductor membrane platform is that it allows broadband non-trivial generation in telecommunication region below the light line and thus enables robust photonic routing in waveguides even with sharp bends. We analytically and numerically investigate the bandstructure of the Kagome photonic crystals and show that the valley-dependent edge states can be categorized into two regions, i.e., Region I ($v_p \times v_g \leq 0$) and Region II ($v_p \times v_g > 0$), where v_p and v_g are phase velocity and group velocity, respectively. Edge modes in Region I have low propagation and bend loss while the edge modes in Region II have high propagation and bend loss, which results in the coexistence of the ring-resonator modes and the Fabry–Pérot resonator modes in the proposed triangular-type KVP cavities. It is worth to note that the edge modes in both regions are topological because they originate from the nontrivial topological charges at the K/K' points in the extended parameter space in contrast to typical quantum Hall effect topological insulators.[47]

We explore topologically protected laser cavities based on the four-level two-electron model and evaluate the robustness and dynamics of the lasing cavities by studying population inversion, lasing spectra, mode field profiles, and light-in light-out (*L*-*L*) responses. To date tight-binding model is widely used to design and analyse gain and lasing behaviour of topological insulator lasers.[30, 31] Our work suggests that the FDTD-based four-level two-electron model offers a powerful alternative platform to study laser performance of topological insulator cavities with arbitrary geometry. Our study helps understanding the interplay between non-Hermiticity and topology, and more importantly provides a new scheme to explore compact all-dielectric topological lasers that can be easily integrated to other passive or active photonic devices by the well-established semiconductor photonic integrated circuit technologies.

Finally, we stress that clockwise (CW) and counterclockwise (CCW) laser edge modes

coexist in the present KVP cavities. Based on the present work, selectively excitation of the CW and CCW modes is possible by nonuniform pumping of the KVP cavity coupled to a waveguide coupler.

Methods

Numerical simulations. The TE-like electromagnetic bandstructure of KVPs based on semiconductor slab were obtained from 3-D MIT Photonic Bands (MPB) software.[48] We retrieve the Berry curvature $F(k)$ from the MPB simulations by scanning wave vector k in the first Brillion zone based on the equation of $F(k) = \nabla_k \times i < u_k|\nabla_k u_k >$, where u_k is the periodic function of the magnetic field $H_z = e^{i\vec{k}\cdot\vec{R}}u_k(\vec{r})$. We characterize the topology of the KVPs by valley Chern number $C_V=C_K–C_{K'}$, where C_K ($C_{K'}$) are Chern number from integration over half of the first Brillouin zone around valley K (K′). We also developed tight binding model and derived the effective Hamiltonian to investigate the topological characteristics of KVP systems (for more details, sections A and B in the Supporting Information). We optimized the band structure of the edge states by scanning geometrical diameters to have as broad wavelength range of edge modes as possible in the telecommunication regime (Figure S4 in Supporting Information).

The projected band structures (Figure 1e) of the topological waveguides were obtained from full-wave three-dimensional (3-D) Finite-difference time-domain (FDTD) (Lumerical software) calculations of a supercell that consists of both the negatively and positively perturbed KVPs. The supercell structure has single period along x direction and 34 periods along y direction, with Bloch boundary conditions, perfectly matched layer boundary conditions and symmetric boundary conditions being applied to FDTD simulation boundaries in x, y, and z directions, respectively. Randomly distributed electrical dipoles are used to excite Bloch modes. Since the time domain signal $E(t) \propto e^{i(\omega+i\gamma)t}$ in FDTD method, the envelope of the decaying signal is determined by $\ln(|E(t)|)$ and thus we can retrieve the decay slope of the edge states (Figure 1f)

using equation of $|(\ln|E(t_2)|-\ln|E(t_1))|/|t_2-t_1|$, where ω, γ and t_1 (t_2) are angular frequency, decay constant and time, respectively.

The simulations of light propagation and field distribution of the edge states in the KVP waveguides were carried out by exciting edge modes with a circular polarized light source placed in specified locations in FDTD modelling (Figure 2). Transmission spectra of the bended waveguide were implemented by normalizing the waveguide to the straight waveguide with the same geometrical parameters (Figure S6 in the Supporting Information).

To get accurate Q factor for the triangular KVP cavities, we placed 11 electrical dipoles randomly near one of the cavity edges (see the star symbol in Figure 3a) to excite all the resonant mode. These dipoles have random phases and excite lights at wavelengths of 1.4 μm-1.6 μm. We put 12 monitors randomly near the cavity edge to record the electrical filed. We extract the slope of the envelope of the decaying light signal in the cavities to derive Q factor by averaging the signal from all the monitors. The FDTD simulation time was 100 ps. Perfectly matched layer boundary conditions were applied to the FDTD boundaries in x and y directions, and symmetric boundary conditions were used for the boundary in z direction.

FSR of the ring-resonator modes was obtained by $\Delta\lambda_{FSR}=\lambda^2/(n_g L_{cavity})$, where λ is light wavelength, n_g is group index and L_{cavity} is the effective length of light propagating in the cavity, respectively. n_g is equal to $c\frac{\partial k}{\partial \omega}$ and thus can be derived from the band structure of the topological waveguide in Figure 1e. Here, c is velocity of light, k is wave number and ω is angular frequency of light. In the numerical simulations, we did not consider the material dispersion of InGaAsP. The propagation loss α of the cavity edge modes is calculated by $\alpha = \frac{2\pi n_g}{Q\lambda}$,[49, 50] where n_g, Q, and λ are the group index, Q factor, and the resonate wavelength of the edge mode, respectively.

Four-level two-electron model. We implemented the dynamics of the electron transition and the population intensity modelling **of** the topological cavities by four-level two-electron model[51] based on 3-D FDTD method (Lumerical software). The four-level atomic system is considered as two coupled dipole oscillators P_a **(**formed by Level 1 and Level 2**)** and P_b (formed by Level 0 and Level 3) with angular frequency of ω_a and ω_b, and dephasing rate γ_a and γ_b (Figure 4b), respectively. N_i is electron population density probability in Level i and τ_{ij} (i, j=0,1,2,3) is the decay time constant between levels i and j. The parameters for the gain material InGaAsP in the model (Figures 4 and 5) are ω_a=1.26×10^{15} Hz and ω_b=1.77×10^{15} Hz, γ_a=1.68×10^{14} Hz, γ_b=1×10^{12} Hz, τ_{30}=τ_{21}=3×10^{-10} s, τ_{32}=τ_{10}=1×10^{-13} s.[51, 52] We use a continuous wave laser with a Gaussian shape intensity profile (Figure 4(a)) at wavelength of 1064 nm to pump the KVP cavities to excite topological laser modes in telecommunication region. The pump laser is placed 1 μm away from the cavity surface and has a waist radius of 12 μm to pump both the inside and outside of the cavities. In the FDTD-based four-level two-electron simulations, we place a frequency-domain monitor at one of the cavity edges and record the electric field components (i.e., E_x, E_y, and E_z) of the monitor to derive the electric field amplitude (i.e., $|E|^2$=$|E_x|^2$+$|E_y|^2$ +$|E_z|^2$) as the output intensity of the generated edge mode lasers. By scanning the intensity of the pump laser, we obtain the normalized light-in light-out (L-L) curve of the lasers (Figure 4f).

ASSOCIATED CONTENT

Supporting Information

Supporting Information Available: *derivation of effective Hamiltonian; Berry curvature and valley Chern number; optimization of KVPs; band structure and field distribution of KVPs*.

AUTHOR INFORMATION

Corresponding Author

* Email: OhS2@cardiff.ac.uk

Author Contributions

S.S.O. conceived the idea and supervised the project. Y.G. and S.W. conducted the designs and simulations. A.J.B. and D.L.H. helped with result analysis. All the authors contributed to the discussions and the preparation of the manuscript.

ACKNOWLEDGEMENTS

The work is part-funded by the European Regional Development Fund through the Welsh Government (80762-CU145 (East)).

REFERENCES

1. Lu, L.; Joannopoulos J. D.; Soljacic M. Topological photonics, *Nat. Photonics* **2014**, *8,* 821-829.
2. Ozawa, T.; Price H. M.; Amo A.; Goldman N.; Hafezi M.; Lu L.; Rechtsman M. C.; Schuster D.; Simon J.; Zilberberg O.; Carusotto I. Topological photonics, *Rev. Mod. Phys.* **2019**, *91,* 015006.
3. Zhong, H.; Li Y.; Song D.; Kartashov Y. V.; Zhang Y.; Zhang Y.; Chen Z. Topological Valley Hall Edge State Lasing. Preprint at arXiv:1912.13003 (2019).
4. Kruk, S.; Poddubny A.; Smirnova D.; Wang L.; Slobozhanyuk A.; Shorokhov A.; Kravchenko I.; Luther-Davies B.; Kivshar Y. Nonlinear light generation in topological nanostructures, *Nat. Nanotechnol.* **2019**, *14,* 126–130.
5. Hafezi, M.; Demler E. A.; Lukin M. D.; Taylor J. M. Robust optical delay lines with topological protection, *Nat. Phys.* **2011**, *7,* 907-912.
6. Zhao, H.; Qiao X. D.; Wu T. W.; Midya B.; Longhi S.; Feng L. Non-Hermitian

topological light steering, *Science* **2019**, *365,* 1163-1166.

7. Cheng, X. J.; Jouvaud C.; Ni X.; Mousavi S. H.; Genack A. Z.; Khanikaev A. B. Robust reconfigurable electromagnetic pathways within a photonic topological insulator, *Nat. Mater.* **2016**, *15,* 542–548.
8. Wang, Z.; Chong Y. D.; Joannopoulos J. D.; Soljacic M. Observation of unidirectional backscattering-immune topological electromagnetic states, *Nature* **2009**, *461,* 772-775.
9. Rechtsman, M. C.; Zeuner J. M.; Plotnik Y.; Lumer Y.; Podolsky D.; Dreisow F.; Nolte S.; Segev M.; Szameit A. Photonic Floquet topological insulators, *Nature* **2013**, *496,* 196-200.
10. Hafezi, M.; Mittal S.; Fan J.; Migdall A.; Taylor J. M. Imaging topological edge states in silicon photonics, *Nat. Photonics* **2013**, *7,* 1001-1005.
11. Mittal, S.; Fan J.; Faez S.; Migdall A.; Taylor J. M.; Hafezi M. Topologically Robust Transport of Photons in a Synthetic Gauge Field, *Phys. Rev. Lett.* **2014**, *113,* 087403
12. Umucalılar, R. O.; Carusotto I. Artificial gauge field for photons in coupled cavity arrays, *Phys. Rev. A.* **2011**, *84,* 043804.
13. Wu, L. H.; Hu X. Scheme for Achieving a Topological Photonic Crystal by Using Dielectric Material, *Phys. Rev. Lett.* **2015**, *114,* 223901
14. Peng, S. Y.; Schilder N. J.; Ni X.; van de Groep J.; Brongersma M. L.; Alu A.; Khanikaev A. B.; Atwater H. A.; Polman A. Probing the Band Structure of Topological Silicon Photonic Lattices in the Visible Spectrum, *Phys. Rev. Lett.* **2019**, *122,* 117401
15. Yang, Y. T.; Xu Y. F.; Xu T.; Wang H. X.; Jiang J. H.; Hu X.; Hang Z. H. Visualization of a Unidirectional Electromagnetic Waveguide Using Topological Photonic Crystals Made of Dielectric Materials, *Phys. Rev. Lett.* **2018**, *120,* 217401
16. Barik, S.; Karasahin A.; Flower C.; Cai T.; Miyake H.; DeGottardi W.; Hafezi M.; Waks E. A topological quantum optics interface, *Science* **2018**, *359,* 666-668.

17. Gorlach, M. A.; Ni X.; Smirnova D. A.; Korobkin D.; Zhirihin D.; Slobozhanyuk A. P.; Belov P. A.; Alu A.; Khanikaev A. B. Far-field probing of leaky topological states in all-dielectric metasurfaces, *Nat. Commun.* **2018**, *9,* 909.

18. Mehrabad, M. J.; Foster A. P.; Dost R.; Clarke E.; Patil P. K.; Farrer I.; Heffernan J.; Skolnick M. S.; Wilson L. R. A Semiconductor Topological Photonic Ring Resonator, *arXiv:1910.07448* **2019**.

19. Ma, T.; Shvets G. All-Si valley-Hall photonic topological insulator, *New. J. Phys.* **2016**, *18,* 025012.

20. Dong, J. W.; Chen X. D.; Zhu H. Y.; Wang Y.; Zhang X. Valley photonic crystals for control of spin and topology, *Nat. Mater.* **2017**, *16,* 298–302.

21. Chen, X. D.; Zhao F. L.; Chen M.; Dong J. W. Valley-contrasting physics in all-dielectric photonic crystals: Orbital angular momentum and topological propagation, *Phys. Rev. B.* **2017**, *96,* 020202(R).

22. Gao, F.; Xue H. R.; Yang Z. J.; Lai K. F.; Yu Y.; Lin X.; Chong Y. D.; Shvets G.; Zhang B. L. Topologically protected refraction of robust kink states in valley photonic crystals, *Nat. Phys.* **2018**, *14,* 140–144.

23. Wu, X. X.; Meng Y.; Tian J. X.; Huang Y. Z.; Xiang H.; Han D. Z.; Wen W. J. Direct observation of valley-polarized topological edge states in designer surface plasmon crystals, *Nat. Commun.* **2017**, *8,* 1304

24. Noh, J.; Huang S.; Chen K. P.; Rechtsman M. C. Observation of Photonic Topological Valley Hall Edge States, *Phys. Rev. Lett.* **2018**, *120,* 063902

25. Kang, Y. H.; Ni X.; Cheng X. J.; Khanikaev A. B.; Genack A. Z. Pseudo-spin-valley coupled edge states in a photonic topological insulator, *Nat. Commun.* **2018**, *9,* 3029

26. Shalaev, M. I.; Walasik W.; Tsukernik A.; Xu Y.; Litchinitser N. M. Robust topologically protected transport in photonic crystals at telecommunication

wavelengths*, Nat. Nanotechnol.* **2019**, *14,* 31–34.

27. He, X. T.; Liang E. T.; Yuan J. J.; Qiu H. Y.; Chen X. D.; Zhao F. L.; Dong J. W. A silicon-on-insulator slab for topological valley transport*, Nat. Commun.* **2019**, *10,* 872

28. Deng, W. M.; Chen X. D.; Chen W. J.; Zhao F. L.; Dong J. W. Vortex index identification and unidirectional propagation in Kagome photonic crystals*, Nanophotonics* **2019**, *8,* 833-840.

29. Bahari, B.; Ndao A.; Vallini F.; El Amili A.; Fainman Y.; Kante B. Nonreciprocal lasing in topological cavities of arbitrary geometries*, Science* **2017**, *358,* 636-639.

30. Harari, G.; Bandres M. A.; Lumer Y.; Rechtsman M. C.; Chong Y. D.; Khajavikhan M.; Christodoulides D. N.; Segev M. Topological insulator laser: Theory*, Science* **2018**, *359,* eaar4003.

31. Bandres, M. A.; Wittek S.; Harari G.; Parto M.; Ren J. H.; Segev M.; Christodoulides D. N.; Khajavilchan M. Topological insulator laser: Experiments*, Science* **2018**, *359,* eaar4005.

32. Zhao, H.; Miao P.; Teimourpour M. H.; Malzard S.; El-Ganainy R.; Schomerus H.; Feng L. Topological hybrid silicon microlasers*, Nat. Commun.* **2018**, *9,* 981.

33. Parto, M.; Wittek S.; Hodaei H.; Harari G.; Bandres M. A.; Ren J. H.; Rechtsman M. C.; Segev M.; Christodoulides D. N.; Khajavikhan M. Edge-Mode Lasing in 1D Topological Active Arrays*, Phys. Rev. Lett.* **2018**, *120,* 113901.

34. Yao, R.; Li H.; Zheng B.; An S.; Ding J.; Lee C.-S.; Zhang H.; Guo W. Electrically Tunable and Reconfigurable Topological Edge State Lasers*, arXiv:1804.01587* **2018**.

35. St-Jean, P.; Goblot V.; Galopin E.; Lemaitre A.; Ozawa T.; Le Gratiet L.; Sagnes I.; Bloch J.; Amo A. Lasing in topological edge states of a one-dimensional lattice*, Nat. Photonics* **2017**, *11,* 651–656.

36. Han, C.; Lee M.; Callard S.; Seassal C.; Jeon H. Lasing at topological edge states in a

photonic crystal L3 nanocavity dimer array*, Light Sci. Appl.* **2019**, *8,* 40.

37. Ota, Y.; Katsumi R.; Watanabe K.; Iwamoto S.; Arakawa Y. Topological photonic crystal nanocavity laser*, Commun. Phys.* **2018**, *1,* 86.

38. Shao, Z. K.; Chen H. Z.; Wang S.; Mao X. R.; Yang Z. Q.; Wang S. L.; Wang X. X.; Hu X.; Ma R. M. A high-performance topological bulk laser based on band-inversion-induced reflection*, Nat. Nanotechnol.* **2019**, doi:10.1038/s41565-019-0584-x.

39. Zhong, H.; Li Y.; Song D.; Kartashov Y. V.; Zhang Y.; Zhang Y.; Chen Z. Topological Valley Hall Edge State Lasing. Preprint at arXiv:1912.13003 (2019).

40. Zeng, Y.; Chattopadhyay U.; Zhu B.; Qiang B.; Li J.; Jin Y.; Li L.; Davies A. G.; Linfield E. H.; Zhang B.; Chong Y.; Wang Q. J. Electrically pumped topological laser with valley edge modes*, Nature* **2020**, *578,* 246-250.

41. Kim, K. H.; Hwang M. S.; Kim H. R.; Choi J. H.; No Y. S.; Park H. G. Direct observation of exceptional points in coupled photonic-crystal lasers with asymmetric optical gains*, Nat. Commun.* **2016**, *7,* 13893

42. Lodahl, P.; Mahmoodian S.; Stobbe S.; Rauschenbeutel A.; Schneeweiss P.; Volz J.; Pichler H.; Zoller P. Chiral quantum optics*, Nature* **2017**, *541,* 473-480.

43. Wong, S.; Saba M.; Hess O.; Oh S. S. Gapless unidirectional photonic transport using all-dielectric kagome lattices*, Phys. Rev. Res.* **2020**, *2,* 012011.

44. Oh, S. S.; Lang B.; Beggs D. M.; Huffaker D. L.; Saba M.; Hess O. Chiral Light-matter Interaction in Dielectric Photonic Topological Insulators*, CLEO Pacific Rim Conference 2018* **2018**, Th4H.5.

45. Bogaerts, W.; De Heyn P.; Van Vaerenbergh T.; De Vos K.; Selvaraja S. K.; Claes T.; Dumon P.; Bienstman P.; Van Thourhout D.; Baets R. Silicon microring resonators*, Laser Photonics Rev.* **2012**, *6,* 47-73.

46. Sun, X.-C.; Hu X. Topological Ring-Cavity Laser Formed by Honeycomb Photonic

Crystals*, arXiv:1906.02464* **2019**.

47. Saba, M.; Wong S.; Elman M.; Oh S. S.; Hess O. Nature of topological protection in photonic spin and valley Hall insulators*, Phys. Rev. B.* **2020**, *101,* 054307.

48. Johnson, S. G.; Joannopoulos J. D. Block-iterative frequency-domain methods for Maxwell's equations in a planewave basis*, Opt. Express* **2001**, *8,* 173-190.

49. Rabiei, P.; Steier W. H.; Zhang C.; Dalton L. R. Polymer micro-ring filters and modulators*, J. Lightwave Technol.* **2002**, *20,* 1968.

50. Griffith, A.; Cardenas J.; Poitras C. B.; Lipson M. High quality factor and high confinement silicon resonators using etchless process*, Opt. Express* **2012**, *20,* 21341-21345.

51. Chang, S. H.; Taflove A. Finite-difference time-domain model of lasing action in a four-level two-electron atomic system*, Opt. Express* **2004**, *12,* 3827-3833.

52. Zhukovsky, S. V.; Chigrin D. N.; Lavrinenko A. V.; Kroha J. Switchable lasing in multimode microcavities*, Phys. Rev. Lett.* **2007**, *99,* 073902.

Supporting Information

Topological Insulator Laser Using Valley-Hall Photonic Crystals

*Yongkang Gong, Stephan Wong, Anthony J. Bennett, Diana L. Huffaker and Sang Soon Oh**

*Email: OhS2@cardiff.ac.uk

A. Derivation of Effective Hamiltonian

In this section, we develop a tight binding model for the proposed KVPs. We calculate the field distribution $|H_z|$ of the perturbed KVPs using MPB software. Figure S1 shows that electromagnetic mode around a hole couples to the other two holes in the same primitive cell (i.e., intracell coupling) and couples to the holes in the nearest neighboring primitive cells as well (i.e., intercell coupling). For the negatively perturbed KVPs, the intracell coupling is stronger than the intercell coupling (Figure S1a), which is the opposite to the case of the positively perturbed KVPs (Figure S1b). Therefore, we can consider our KVPs as 2-D tight binding system with each cell having three sites and consider both the intracell and the intercell coupling, as schematically shown in Figure S2(a). Under the tight binding approximation, Hamiltonian of the KVPs can be given by the following

$$\widehat{H}|\psi = E|\psi\rangle, \tag{S1}$$

where E is eigenvalue and ψ is the eigenvector. A state that sits on a site σ ($\sigma = A, \mathrm{B}, \mathrm{C}$) in the (m, n) unit cell of our system is denoted by $|m, n, \sigma\rangle$. Thanks to translation symmetry of the system, any state $|\psi_{\mathrm{k}}\rangle$ can be written as

$$|\psi_{\mathrm{k}}\rangle = \sum_{m,n} e^{ik\cdot R}(c_A|m, n, A\rangle + c_B|m, n, B\rangle + c_C|m, n, C\rangle) \tag{S2}$$

Here, $R = m\overrightarrow{R_1} + n\overrightarrow{R_2}$ is the translation lattice vector and c_σ is a constant to normalize the state $|\psi_{\mathrm{k}}\rangle$.

With the nearest-neighbour approximation, the Hamiltonian of the whole lattice can be constructed by considering both intracell and intercell hopping as

$$\hat{H} = \hat{H}_{intra} + \hat{H}_{inter}, \tag{S3}$$

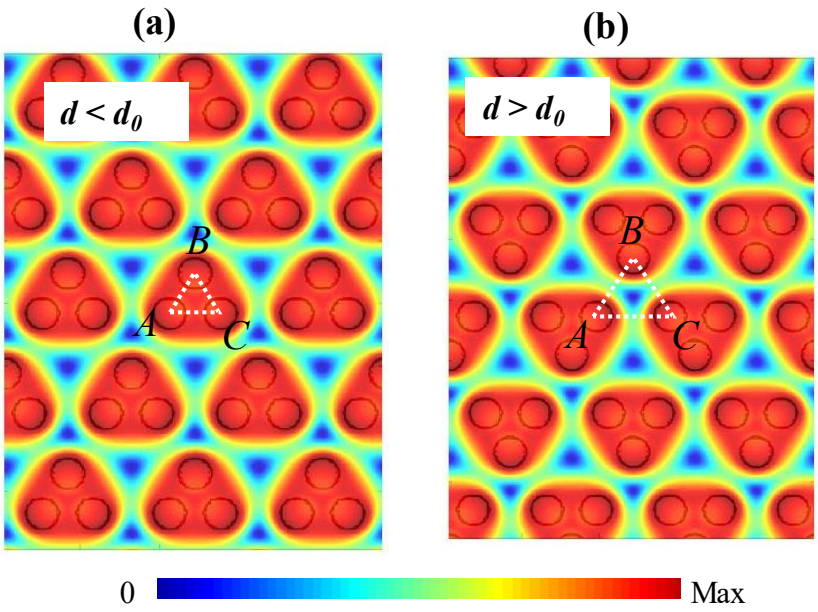

Figure S1. Field distribution $|H_z|$ of a) the negatively and b) positively perturbed 3-D KVPs at K point in the first band at z=0 μm plane. Labels "*A*", "*B*" and "*C*" indicate the three holes in a primitive cell. The black circles represent the outline of holes. The parameters in the calculation are the same to Figure 1 in the main text.

where the intracell hopping Hamiltonian $\hat{H}_{intra}$ and intercell hopping Hamiltonian $\hat{H}_{inter}$ equal to

$$\hat{H}_{intra} = -v \sum_{m,n} e^{ik\cdot R} \left(|m,n,B><m,n,A| + |m,n,C><m,n,B| + |m,n,A><m,n,C| + h.c.\right), \tag{S4}$$

$$\hat{H}_{inter} = -w \sum_{m,n} e^{ik\cdot R} \left(|m,n+1,B><m,n,A| + |m+1,n,C><m,n,B| + |m+1,n-1,A><m,n,C| + h.c.\right). \tag{S5}$$

Here, k is the wave vector, v (w) are the intracell (intercell) hopping strength, and *h.c.* denotes the Hermitian conjugate of the previous three states in equations S4 and S5. The eigenvalue equation can be reduced to the effective eigenvalue problem:

$$\hat{H}_{eff}(k)|\phi\rangle = \varepsilon(k)|\phi\rangle, \tag{S6}$$

where $\varepsilon(k)$ is energy eigenvalue, $|\phi\rangle = (\phi_A, \phi_B, \phi_C)$ is the corresponding three-component

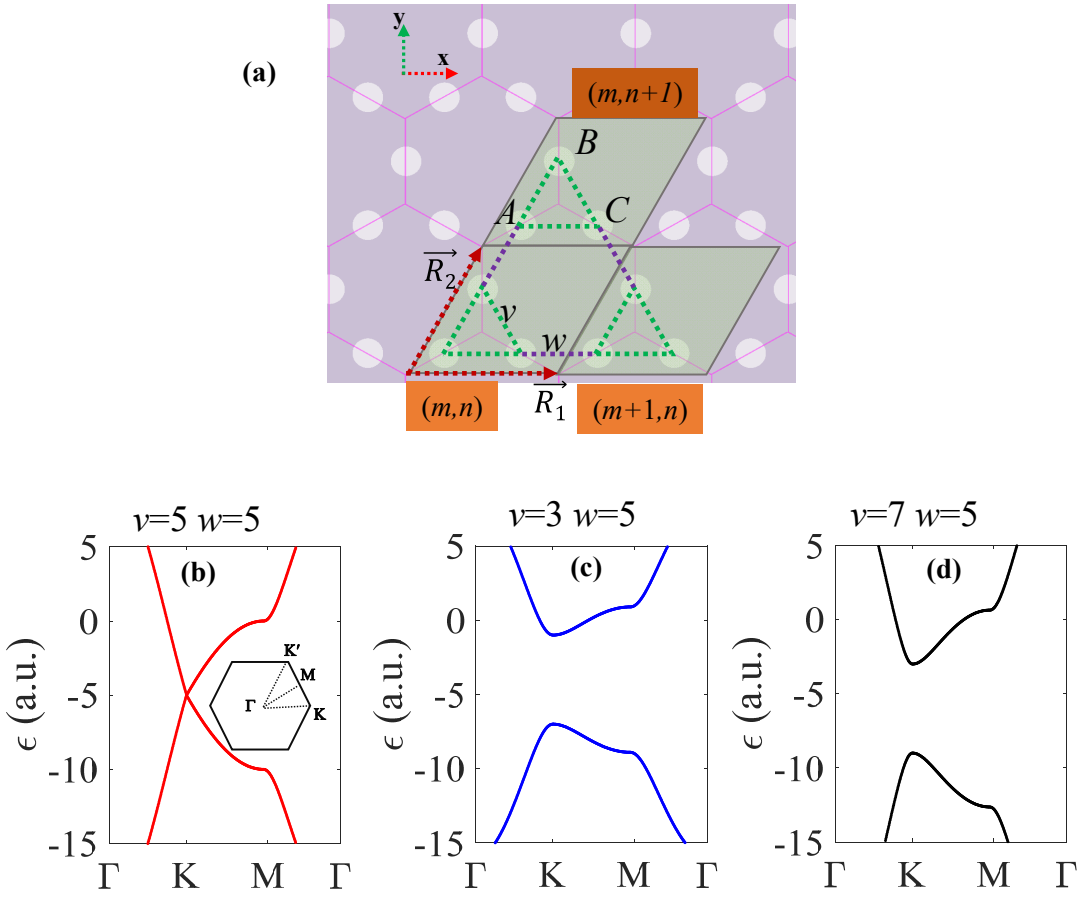

Figure S2. Tight binding approximation for effective Hamiltonian derivation. a) Schematic illustration of the tight binding model for the system under study. The structure has triangular lattice with unit cell composed of three sites *A*, *B* and *C*. Lattice unit vectors are $\overrightarrow{R_1}$ and $\overrightarrow{R_2}$. *v* represents the intracell hopping strength of the three sites and *w* labels intercell hopping strength between two neighboring unit cells. (*m*,*n*) represents the location of unit cells. b)-d) Band structure of the unperturbed, negatively perturbed and positively perturbed KVPs, respectively. Bandgap opening occurs in the vicinity of K point when KVPs are perturbed, which agrees well with the results in Figure 1b in the main text.

eigenvector, and $\widehat{H}_{eff}$ is the effective Hamiltonian that reads

$$\widehat{H}_{eff}(\vec{k}) = \begin{pmatrix} 0 & -\left(v + we^{i\vec{k}\cdot\overrightarrow{R_2}}\right) & -\left(v + we^{-i\vec{k}\cdot(\overrightarrow{R_1}-\overrightarrow{R_2})}\right) \\ -\left(v + we^{-i\vec{k}\cdot\overrightarrow{R_2}}\right) & 0 & -\left(v + we^{-i\vec{k}\cdot\overrightarrow{R_1}}\right) \\ -\left(v + we^{i\vec{k}\cdot(\overrightarrow{R_1}-\overrightarrow{R_2})}\right) & -\left(v + we^{i\vec{k}\cdot\overrightarrow{R_1}}\right) & 0 \end{pmatrix}. \quad \text{(S7)}$$

By solving the effective Hamiltonian system based on Eqs. S6 and S7, we can obtain the band structure and the Berry curvature of the proposed KVPs.

We calculate the eigenvalue of the developed tight binding system by solving Equation S6. We note from Figure S2b that there is a linear degeneracy at the K point when the Kagome structure is unperturbed (i.e., v=w). The degeneracy can be lifted in both the negatively perturbed (i.e., v>w) and positively perturbed (i.e., v<w) KVPs and bandgap appears at the vicinity of K point, as shown in Figures S2(a) and S2(b). The results agree with the band structure analysis in Figure 2b in the main text, which validates the effective Hamiltonian we derived.

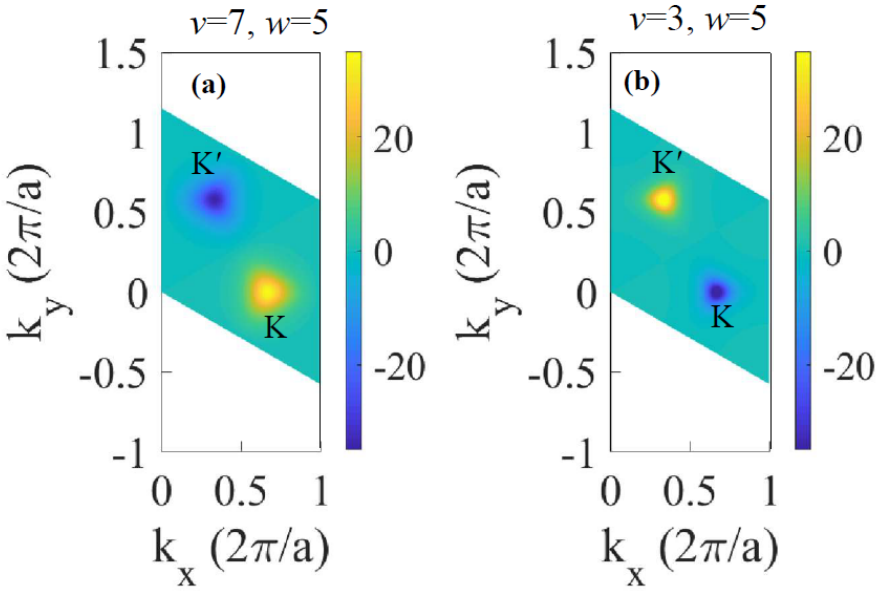

Figure S3. Berry curvature of a) the negatively and b) positively perturbed KVPs. The Berry curvature is analytically obtained from Equation S8.

B. Berry Curvature and Valley Chern number

Based on the effective Hamiltonian derived in the previous section, we can obtain the Berry curvature and the Chern number. One can analytically derive the Berry curvature $F(k)$ for eigenvalue $\varepsilon_m(k)$ corresponding to an eigenvector $|\Phi_m\rangle$ at a certain k point: [1]

$$F(k) = -\mathrm{Im}\left(\sum_{m\neq n} \frac{<\phi_{n,k}|(\nabla_k \hat{H}_{eff})|\phi_{m,k}>\times<\phi_{m,k}|(\nabla_k \hat{H}_{eff})|\phi_{n,k}>}{(\varepsilon_n(k)-\varepsilon_m(k))^2}\right). \quad \text{(S8)}$$

Here, Im means imaginary part of the equation. Based on Equation S8, we calculate the Berry curvature of the first band of the perturbed KVPs over the primitive unit cell (Figure S3). We notice that the Berry curvature has opposite sign at the K and K' points: the negatively perturbed KVPs have negative Berry curvature at K' and positive Berry curvature at K, while the positively perturbed KVPs have positive Berry curvature at K' and negative Berry curvature at K. The results are in consistent with the calculated Berry curvature in Figures 1d and 1e in the main text.

Based on the obtained Berry curvature we can characterize the topology of the KVP systems by valley Chern number $C_V=C_K-C_{K'}$, [2, 3] where C_K ($C_{K'}$) are from integration of Berry curvature around valley K (K′). Apparently, the negatively perturbed KVPs have negative $C_{K'}$ and positive C_K due to negative (positive) Berry curvature around K (K′), and thereby possess of negative valley Chern number (i.e., $C_V<0$). On the contrary, the positively perturbed KVPs have positive valley Chern number (i.e., $C_V>0$). Therefore, the positively and negatively perturbed KVPs have different topology, and topological edge states are guaranteed at their boundary as shown in Figure 1a in the main text.

C. Optimization of KVPs

We optimize the edge states of the proposed 3-D KVPs by scanning slab height h, lattice length a, and hole diameter D, so that the central wavelength of edge states λ_0 lies in telecommunication region and wavelength range of edge states $\Delta\lambda$ is as broad as possible. Figure S4 demonstrates that λ_0 increase with slab thickness and lattice and decreases with hole

diameter.

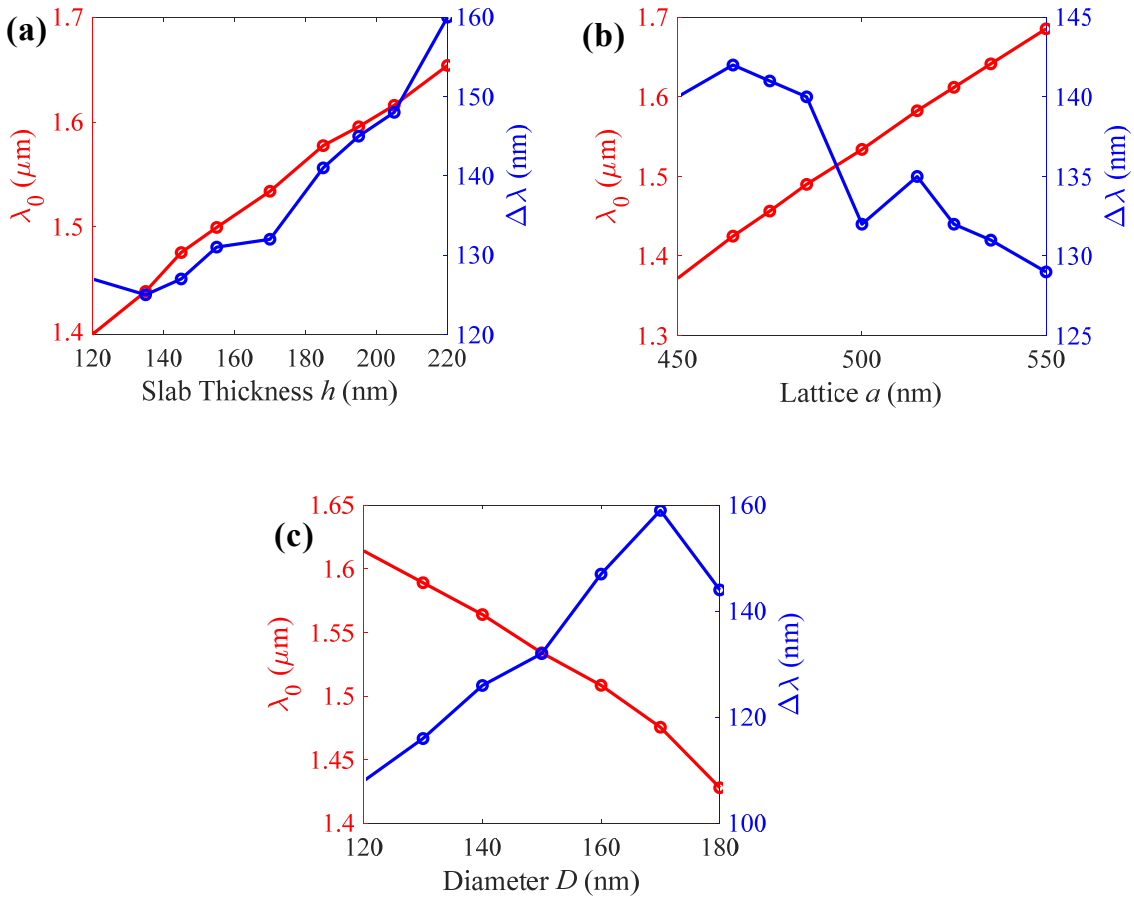

Figure S4. Optimization of the proposed KVPs edge states. a) Dependence of λ_0 and $\Delta\lambda$ on structure slab thickness. The other parameters are a=500 nm and D=150 nm. b) Dependence of λ_0 and $\Delta\lambda$ on structure lattice length. The other parameters are h=170 nm and D=150 nm. c) Dependence of λ_0 and $\Delta\lambda$ on hole diameter. The other parameters are h=170 nm, and a=500 nm.

D. Band structure and field distribution of KVPs

We plot field distribution $|E|^2$ of light propagation in the Z-bended waveguide (see Figure 2b in the main text) at edge mode wavelength of 1550 nm in both *xy* and *xz* planes. Figure S5 illustrates that light propagates smoothly around the sharp corners and is well confined at the out-of-plane because of the edge modes being below light line.

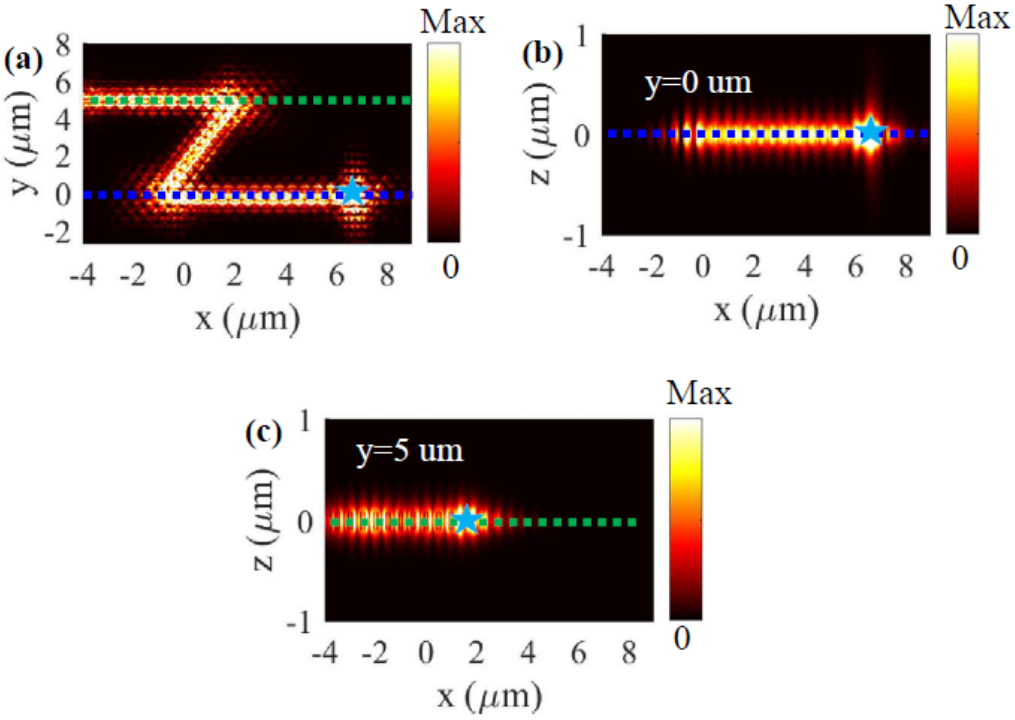

Figure S5. a) Field distribution $|E|^2$ of light propagation in Z-bended waveguide in *xy* plane at wavelength of 1550 nm. The star symbol indicates circular polarized source exciting unidirectional light propagation to the left of the waveguide. b)-c) Field distribution $|E|^2$ in the *xz* plane at the locations indicated by the blue and green dashed plane marked in a), respectively.

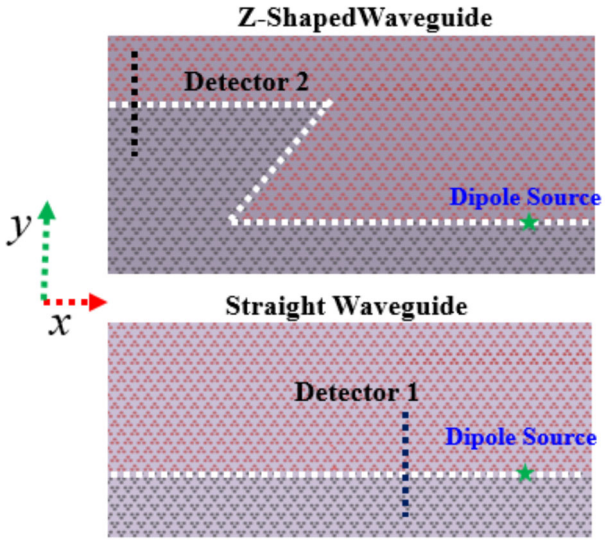

Figure S6. FDTD calculation of the transmissivity spectrum of the Z-shaped waveguide. The transmissivity spectrum is obtained by normalizing the light power recorded from Detector 2

in the Z-shaped waveguide (schematically shown in upper figure) to the light power from Detector 1 in the straight waveguide (schematically shown in lower figure). The white lines indicate the geometrical boundary of the perturbed KVPs and the star symbols represent circular polarized dipoles to excite light to the waveguides. The two back dashed lines indicate the location of the detectors in FDTD simulations.

When we alter the topological edge by arranging the positively and negatively perturbed KVPs in the opposite way to Figure 1a in the main text while maintaining geometrical parameters, as depicted in Figure S7(a), although we can still obtain broad edge modes within band gap, the majority of edge modes become lying above the light line (Figure S7(b)).

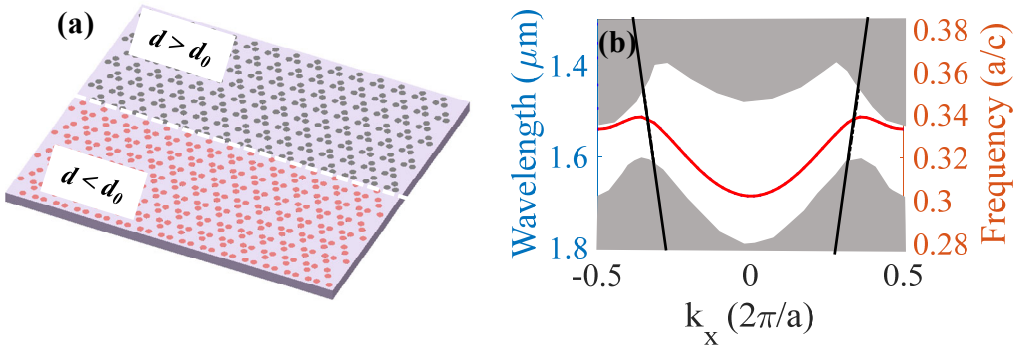

Figure S7. a) Schematic of a topological edge composed of positively and negatively perturbed KVPs. b) Band structure of the topological edge. The geometrical parameters used in this calculation are same to that in Figure 1e in the main text.

E. Q factor of KVP cavities

Figure S8 depicts the dependence of the cavity Q factor on the number of the periods of the surrounding photonic crystals *m*. In the FDTD simulations, perfectly matched layers are applied to the structure boundaries in *x* and *y* directions, and symmetric boundary conditions are used to the boundaries in *z* direction. The Q factor does not change much as long as m is large to confine the field of the edge modes near cavity edges. For example, when cavity length is L=8.5 μm, the Q factor hardly changes when *m* is larger than 13.

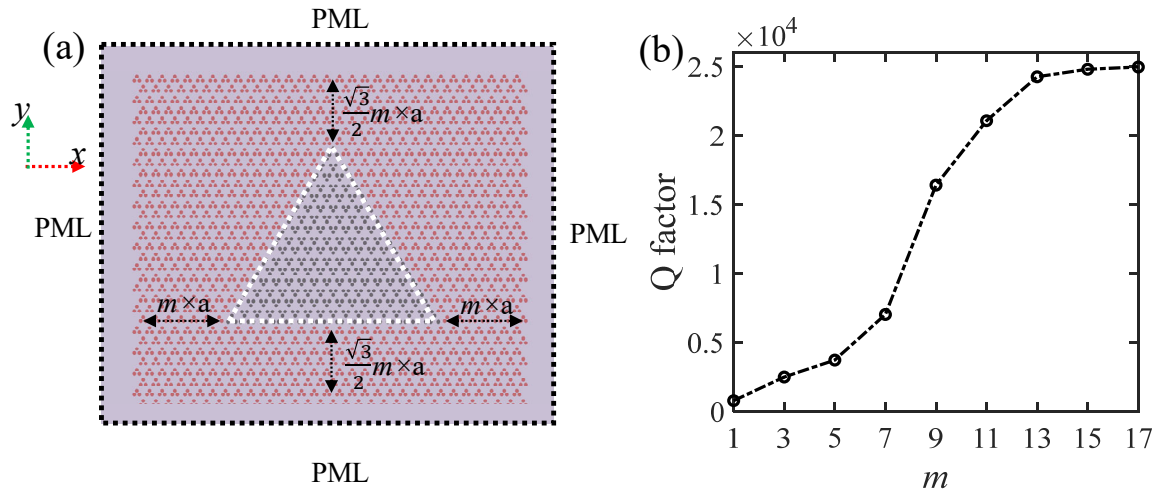

Figure S8. a) Schematic of the KVP cavities for the *Q* factor calculations in 3-D FDTD modeling. The dotted white line represents the cavity edges. The inside and outside of the cavity are the negatively and positively perturbed KVPs, respectively. *a* is the lattice length. (b) Dependence of the *Q* factor on *m*. The cavity length is fixed at *L*=8.5 μm in the simulations. Other geometric parameters are same as that in Figure 3 in the main text.

References

1. M. V. Berry, "Quantal phase factors accompanying adiabatic changes," *Proc. R. Soc. Lond. A,* **1984**, 392, 45.
2. T. Ma, G. Shvets, "All-Si valley-Hall photonic topological insulator," *New. J. Phys*. **2016**, 18, 025012.
3. X. T. He, E. T. Liang, J. J. Yuan, H. Y. Qiu, X. D. Chen, F. L. Zhao, J. W. Dong, "A silicon-on-insulator slab for topological valley transport," *Nat. Commun*. **2019**, 10, 872.